LIF diagnostics of hydroxyl radical in a methanol containing atmospheric-pressure plasma jet*

Mu-Yang Qian(钱沐杨)[1], San-Qiu Liu(刘三秋)[1,†], Xue-Kai Pei(裴学凯)[2], Xin-Pei Lu(卢新培)[2], Jia-Liang Zhang(张家良)[3], and De-Zhen Wang(王德真)[3]

[1] *Department of Physics, Nanchang University, Nanchang* 330031, *China*
[2] *China State Key Laboratory of Advanced Electromagnetic Engineering and Technology, Huazhong University of Science and Technology, Wuhan* 430074, *China*
[3] *School of Physics and Optoelectronic Technology, Dalian University of Technology, Dalian* 116023, *China*

(Received 22 May 2016; revised manuscript received 16 June 2016; published online 25 August 2016)

In this paper, a pulsed-dc CH_3OH/Ar plasma jet generated at atmospheric pressure is studied by laser-induced fluorescence (LIF) and optical emission spectroscopy (OES). A gas–liquid bubbler system is proposed to introduce the methanol vapor into the argon gas, and the CH_3OH/Ar volume ratio is kept constant at about 0.1%. Discharge occurs in a 6-mm needle-to-ring gap in an atmospheric-pressure CH_3OH/Ar mixture. The space-resolved distributions of OH LIF inside and outside the nozzle exhibit distinctly different behaviors. And, different production mechanisms of OH radicals in the needle-to-ring discharge gap and afterglow of plasma jet are discussed. Besides, the optical emission lines of carbonaceous species, such as CH, CN, and C_2 radicals, are identified in the CH_3OH/Ar plasma jet. Finally, the influences of operating parameters (applied voltage magnitude, pulse frequency, pulsewidth) on the OH radical density are also presented and analyzed.

Keywords: atmospheric-pressure plasma jet, hydrocarbon, OH radicals, laser-induced fluorescence

PACS: 52.50.Dg, 52.70.Kz, 82.33.Xj, 52.38.Dx **DOI:** 10.1088/1674-1056/25/10/105205

1. Introduction

Low-temperature atmospheric-pressure plasma jets (LT-APPJs) excited by pulsed-dc power source have attracted considerable attention and shown significant promise in lots of practical applications, including plasma medical, environmental control, and organic synthesis.[1–7] In the listed applications, molecular gases, such as O_2, H_2O, and air are usually admixed into the noble working gas to increase radical species density. Among them, OH is considered to be one of the strongest oxidative species produced in humid-air plasma and a dominant reactive agent in the practical applications. Feed gas humidity and operating parameters are identified as the key factors that strongly influence the OH formation mechanism and absolute density in APPJ. Recently, organic synthesis using methanol as carbon-based organic molecule by LT-APPJs has received more and more attention.[7] Further, the physicochemical mechanism of methanol dissociation is crucial to practical applications. Small fragments, such as OH, CH_3, CH_2OH, and CH_3O, are the direct products of methanol dissociation by energetic electrons and long-life metastable atoms. Therefore, it is of great importance to study the reaction mechanism of OH production in atmospheric CH_3OH/Ar plasma jet.

The measurements of OH absolute density and the effect of water content in working gas on plasma discharge have already been addressed by absorption and/or LIF spectroscopy, and numerical simulation.[8–14] For instance, Bruggeman *et al.*[8] measured the absolute OH densities by broadband UV absorption in atmospheric He/H_2O RF glow discharges and found that OH densities and gas temperatures range between 6×10^{19} m^{-3} and 4×10^{20} m^{-3} and between 345 K and 410 K respectively, for different powers and water content values. Verreycken *et al.*[9] reported OH production in a cold atmospheric-pressure Ar–H_2O RF discharge jet by temporally and spatially resolved LIF. The gas temperature and OH density in the afterglow of pulsed positive corona discharge were also measured using LIF.[10,11] Li *et al.*[12] studied the effect of water addition on the OH radical production by LIF in an Ar–H_2O atmospheric plasma jet. They concluded that the highest density of 1.15×10^{20} m^3 is measured in the closest distance to the plasma core for the case of 0.3% H_2O. Besides, the effect of water content on OH production in an atmospheric helium-air plasma jet is numerically studied by a two-dimensional (2D) fluid model.[13] Liu *et al.*[14] studied the formation mechanism of OH radicals in a pulsed-dc plasma jet by a 2D model and a one-dimensional (1D) discharge model. In most of these studies, the plasma jets were often operated in a humid environment and/or extra water that was added to the working gas

*Project supported by the National Natural Science Foundation of China (Grant Nos. 11465013 and 11375041), the Natural Science Foundation of Jiangxi Province, China (Grant Nos. 20151BAB212012 and 20161BAB201013), and the International Science and Technology Cooperation Program of China (Grant No. 2015DFA61800).

†Corresponding author. E-mail: sqlgroup@ncu.edu.cn

© 2016 Chinese Physical Society and IOP Publishing Ltd

flow.

In this paper, an atmospheric-pressure CH_3OH/Ar plasma jet produced between needle-to-ring electrodes is investigated. The methanol vapor is artificially introduced into the argon working gas through the liquid-gas bubbler system. The LIF diagnostic system is adopted to capture the spatially resolved distribution of OH radicals within a quartz tube and in the plasma afterglow. Optical emission spectroscopy (OES) is used to identify various reactive species in the CH_3OH/Ar plasma jet. Besides, the variation of absolute OH density with operating parameter is also presented and discussed.

2. Experimental setup

A schematic diagram of the experiment set is shown in Fig. 1(a). The plasma jet device consists of needle-to-ring electrodes geometry. A 1.0-mm-diameter tungsten needle electrode is inserted into a 14.5-cm-long quartz tube that has an inner diameter of 8.0 mm and an outer diameter of 10.0 mm and is used as a powered electrode. A 4.0-mm-wide aluminum foil wrapped around the quartz tube surface near the nozzle serves as a grounded electrode. The distance between needle point and grounded aluminum foil is fixed at 6.0 mm. Notice that $z = 0$ indicates the position of the exit nozzle of the quartz tube. To control the methanol vapor content in CH_3OH/Ar gas mixture, a gas-methanol ($\geq 99.5\%$, analytical reagent) bubbler system is proposed. Dry argon gas is split into two channels (labeled by numbers 1 and 2 in Fig. 1(a)), i.e., a main gas channel and a channel which is guided through a methanol reservoir. Behind the bubbler, both argon gas streams are mixed preliminarily in a 50-ml spherical buffer vessel and lead into the quartz tube. In this work, the argon flow rates passing through the main channel and methanol bubbler are both kept constant at 4 slpm and 15 sccm, respectively. The concentration of methanol vapor is directly measured by two small-range mass flow controllers (identified by the letters b and c in Fig. 1(a)). The flow difference between these two MFCs is measured to be about 4.5 sccm. Then, the CH_3OH/Ar volume ratio is determined to be about 0.1%. It is worth noting that the bubbler system is placed in a water bath to adjust the water temperature. When CH_3OH/Ar gas mixture is guided into the quartz tube and high voltage pulses are applied to the HV electrode, a bright plasma discharge is ignited in the needle-to-ring region, and meanwhile, a homogenous plasma jet is produced along the z axis direction and formed in the air opening as shown in Fig. 1(b).

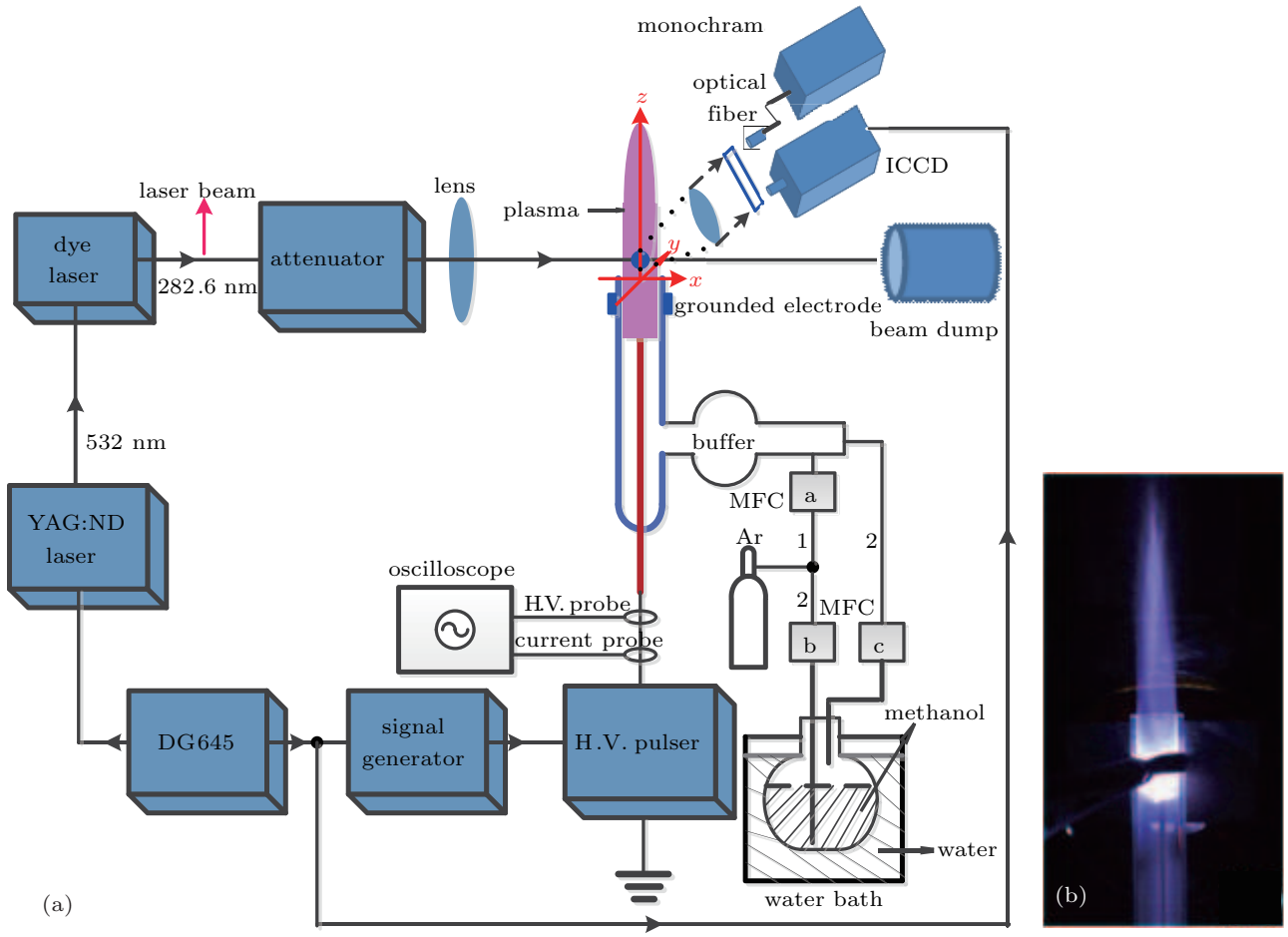


Fig. 1. (color online) (a) Schematic diagram of the experimental setup, (b) a photograph of CH_3OH–Ar plasma jet excited with 8.0 kV, 8.0 kHz, and 1.0-μs pulses, and CH_3OH/Ar ratio of 0.1%. $z = 0$ indicates the position of quartz tube nozzle exit.

The LIF diagnostic system has been described in our previous publications,[14–16] and will be briefly summarized here. A dye laser (Radiant Dyes, NarrowScan) pumped by a YAG: Nd laser (Continuum, SURELITE III-10) is used to excite the OH radicals at 532 nm with 100 μJ per pulse. The laser dye is Rhodamine 6G. The laser wavelength is chosen to be 282.6 nm which is the $P_1(2)$ branch of the OH (A→X) (1→0) band. The laser beam has a frequency of 10 Hz and a pulse duration of 7 ns (FWHM). As can be seen in Fig. 1(a), the laser beam is focused into a 500-μm-diameter spot by using a quartz lens, and then passes through the plasma along the x axis. Being perpendicular to the laser beam, the fluorescence light focused by using a UV lens (Goyo Optical GMUV510540) passes through a narrow-band filter ($\lambda_0 = 309$ nm, FWHM 10 nm), and then captured by an ICCD camera (Princeton Instruments, PIMAX2). In this paper, the exposure time of ICCD is fixed at 50 ns for all imaging measurements. Besides, the OH fluorescence light is an accumulation of 500 pulses. Voltage and current are measured respectively by a high-voltage probe (P6015) and a Pearson current probe (model 2877) via a digital wide band oscilloscope (Tektronix DPO7104). The optical emission spectra are measured by a halfmeter spectrometer (Princeton Instruments Acton SpectraHub 2500i). In this work, the parameters of the power supply are adopted as follows: applied voltage $V_a = 8.0$ kV, pulse frequency $f_p = 8.0$ kHz, and pulse width $t_p = 1.0$ μs, and the temperature of water bath is kept constant at 300 K. Besides, the distance between the intersection of the laser beam and the nozzle is adjustable, which monitors the variation of the operating parameters and is fixed at 1 mm ($z = 1$ mm) unless otherwise stated.

3. Experimental results and discussion

3.1. Electrical and optical characterization

Figure 2 shows the temporal behaviors of the current-voltage waveforms of the plasma discharge. It should be pointed out that the discharge current I_{dis} is the actual discharge current and is obtained by subtracting the displacement current I_{off} from the total discharge current I_{on}. As can be seen, there are two distinct current pulses per voltage pulse. The peak value of positive discharge current is about 0.42 A, which is almost twice as large than that of negative discharge current. It should be pointed out that the negative discharge is related to the feedback electric field induced by the charges, which have accumulated on the quartz tube surface during the positive discharge.

Figures 3(a)–3(a) show OH LIF intensities at five positions in the afterglow of the plasma jet ($z = 1$, 3, 5, 7, and 13 mm). Meanwhile, OH LIF distribution within the needle-to-ring discharge gap is also presented in Fig. 3(f). In this case, the distance from the intersection of plasma and laser beam to the tungsten needle tip is fixed at about 3 mm. In other words, $z = -20$ mm indicates the position of the intersection of the laser beam and the plasma. Notice that these OH fluorescence images are all captured at the time of 1 μs after the falling edge of the voltage pulse. As can be seen in Fig. 3, distinct types of space-resolved behaviors are observed for the OH LIF emission while the plasma propagates inside and outside the nozzle. First, the OH LIF emission intensities are much stronger on both edges as shown in Figs. 3(a)–3(e). In other words, we should observe the ring-shaped emission profiles when we take photographs from the end view. Besides, when the position is farther from the nozzle, the OH LIF emission is weaker and the ring-shaped profile is more pronounced. However, figure 3(f) clearly shows that the OH LIF emission is relatively uniform inside the nozzle. It is worth noting that there is a little laser energy loss due to refraction on the quartz surface. Therefore, a precise comparison between the LIF emission intensity in the afterglow plasma jet and the emission intensity in the needle-to-ring plasma discharge is unreasonable. But, LIF intensity inside the nozzle is indeed stronger than those outside the nozzle.

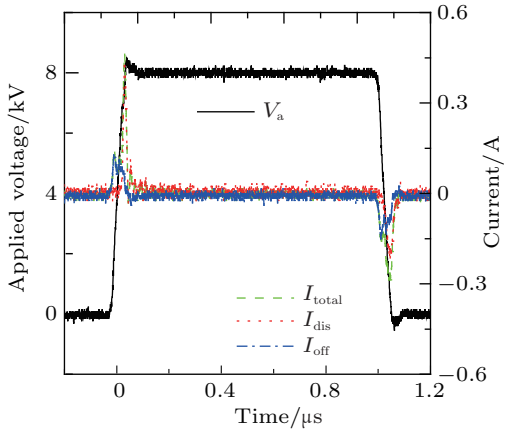


Fig. 2. (color online) Time-dependent typical applied voltage V_a, the total current I_{on} (plasma on), displacement current I_{off} (no plasma), and actual discharge current I_{dis} at CH_3OH/Ar ratio of 0.1%.

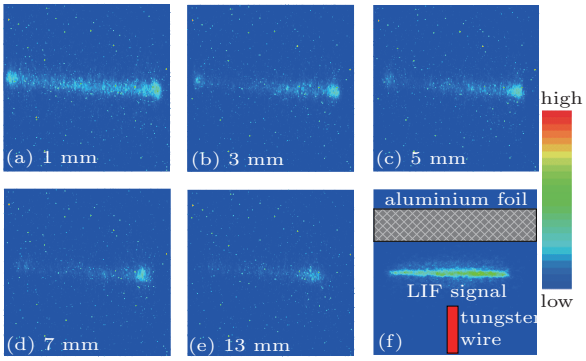


Fig. 3. (color online) Nanosecond images of OH LIF intensity at $z =$ (a) 1 mm, (b) 3 mm, (c) 5 mm, (d) 7 mm, (e) 13 mm, (f) −20 mm (center of needle-to-ring spacing), the grounded aluminum foil and the tungsten wire electrode are also marked. The values of the color scale are normalized. Images are all captured at the time of 1 μs after the falling edge of the voltage pulse.

The ring-shaped OH distributions in the afterglow plasma jets were also reported by previous papers.[12,16,17] The OH radicals can be produced by a large number of mechanisms, which depend on plasma properties. Furthermore, in LT-APPJs discharge with low ionization (10^{-5}–10^{-4}), the main reaction pathways to generating the OH radicals are the electron dissociation of H_2O[18]

$$e + H_2O \rightarrow e + OH + H, \quad k \approx 10^{-11}\ cm^3 \cdot s^{-1}, \tag{1}$$

the dissociation recombination of water ions,

$$e + H_2O^+ \rightarrow OH + H, \quad k \approx 10^{-8} - -10^{-10}\ cm^3 \cdot s^{-1}, \tag{2}$$

and the dissociations by radicals and metastables,[12]

$$O(^1D) + H_2O \rightarrow 2OH, \quad k \approx 2.2 \times 10^{-10}\ cm^3 \cdot s^{-1}, \tag{3}$$

$$Ar^m + H_2O \rightarrow OH + H + Ar, \quad k \approx 4.5 \times 10^{-10}\ cm^3 \cdot s^{-1}, \tag{4}$$

$$N_2^m + H_2O \rightarrow OH + N_2H, \quad k \approx 2.5 \times 10^{-10}\ cm^3 \cdot s^{-1}, \tag{5}$$

$$N_2^m + H_2O \rightarrow OH + N_2(X) + H, \quad k \approx 6.0 \times 10^{-14}\ cm^3 \cdot s^{-1}. \tag{6}$$

However, in our work, there is another channel for the OH production in our methanol containing an atmospheric argon plasma jet. The possible pathways in the CH_3OH/Ar plasma are highly complicated, and the primary plasma reactions are listed in Table 1.[7,19–22] The R1–R7 reactions are the seven initial reaction channels of methanol dissociation. The energy of C–O bonds (3.53 eV) is much less than those of C–H (4.10 eV) and O–H bonds (4.37 eV), which indicates that the selective activation of the C–O bond of methanol will be preferred in CH_3OH/Ar plasma. Thus, additional OH radicals may be produced from the methanol dissociation through the R1 channel ($CH_3OH \rightarrow CH_3 + OH$), which is demonstrated by the fact that OH density in CH_3OH/Ar (0.1% volume ratio) plasma is larger than that in pure argon plasma (data not shown). In our experiment, the trace amount of water molecule existing in argon gas is about 4 ppm, and the methanol vapor content in argon gas is 0.1%. On the other hand, the water vapor content in the air opening is about 1.3%. Therefore, the concentration of water vapor in open air is far more than that inside the nozzle. Actually, the contributions of water dissociation (reaction 1) and methanol vapor dissociation (R1 in Table 1) to the OH radicals production in the afterglow of plasma jet are relatively small, especially at a large distance from the nozzle where low-energy electrons are not sufficient to dissociate methanol molecules (3.53 eV) and water molecules (5.1 eV). Therefore, the ring-shaped OH LIF emission in the afterglow of plasma jet may be ascribed to the production of radicals due to metastables-neutral reactions (reactions 3–6). In other words, it seems possible that OH can be produced in the outer shell of the afterglow plasma jet, where a mixing layer of the working gas and diffused air is formed and water vapor density reaches maximum. However, in the inter-electrode case, the seven channels of methanol dissociation (R1–R7 in Table 1) mentioned above are all the possible pathways. The trace water and methanol vapor molecules are uniformly distributed in argon gas. Therefore, it is reasonable to observe the relatively uniform distribution of OH LIF emission as shown in Fig. 3(f). In summary, inside the nozzle, most of OH radicals come from dissociation of water and methanol vapor contained in the flowing argon gas in the quartz tube, while in the far afterglow of plasma jet, OH radicals may be produced through the reactions of water dissociation with metastalbes.

Table 1. Possible reaction pathways in atmospheric CH_3OH/Ar plasma discharge

R×*n*	Reactions	Calculated energy (eV at 300 K)	References
R1	$CH_3OH \rightarrow CH_3 + OH$	3.53	[7]
R2	$CH_3OH \rightarrow CH_2OH + H$	4.10	[7]
R3	$CH_3OH \rightarrow CH_3O + H$	4.37	[7]
R4	$CH_3OH \rightarrow CH_2O + H_2$	3.84	[7]
R5	$CH_3OH \rightarrow$ *cis*-HCHO + H_2	3.69	[7]
R6	$CH_3OH \rightarrow$ *trans*-HCHO + H_2	3.66	[7]
R7	$CH_3OH \rightarrow {}^1CH_2 + H_2O$	3.63	[7]
R8	$CH_2OH \rightarrow CH_2 + OH$	4.98	[19]
R9	*trans*-HCHO $\rightarrow CH_2O$	1.17	[19]
R10	*trans*-HCHO $\rightarrow$*cis*-HCHO	0.95	[19]
R11	$CH_2O \rightarrow CO + H_2$	3.5	[19]
R12	*cis*-HCHO $\rightarrow CO + H_2$	2.05	[19]
R13	$CH_3OH + H \rightarrow CH_2OH + H_2$	0.46	[19]
R14	$CH_3OH + OH \rightarrow CH_2OH + H_2O$		[20]
R15	$CH_3 + H \rightarrow CH_4$		[21]
R16	$CH_3 + CH_3 \rightarrow CH_3CH_3$		[21]
R17	$CH_2OH + H \rightarrow H_2 + HCHO$		[21]
R18	$CH_2OH + OH \rightarrow H_2O + HCHO$		[21]
R19	$CH_2OH + CH_2OH \rightarrow HOCH_2\text{-}CH_2OH$	2.88	[19]
R20	$CH_3 + CH_2OH \rightarrow CH_3CH_2OH$	3.24	[19]
R21	$CH_3CH_2 + CH_2OH \rightarrow C_3H_7OH$	3.00	[19]
R22	$CH_3CH_2 + OH \rightarrow CH_3CH_2OH$	3.72	[19]

Note: (i) *trans*-HCHO, *cis*-HCHO, and CH_2O are isomers of each other. (ii) The dissociation reactions (R1–R7) are initiated by energetic electrons and/or atomic argon metastables.

OES is used to detect various excited species generated by the CH_3OH/Ar plasma in a wavelength range from 300 nm to 850 nm as shown in Fig. 4. The spectrum is collected from the plasma jet at about 1 mm away from the nozzle exit ($z = 1$ mm). As can be seen in Fig. 4(a), it clearly indicates that in addition to the carbonaceous species lines, there exist the hydroxyl line (309 nm), the molecular nitrogen N_2, the H_α line, and the atomic argon lines in the plasma plume. Figure 4(b) shows the detailed spectrum in a range of 300 nm–600 nm. Three typical carbonaceous species lines, namely CH A–X system ($A^2\Delta \rightarrow X^2\Pi$, 431.3 nm), CN B–X system ($B^2\Sigma \rightarrow X^2\Sigma$, 386.2, 387.1, 388.3 nm), and C_2 swan system ($A^3\Pi \rightarrow X^3\Pi$, 450 nm–600 nm), are clearly present, which may indicate the dissociation of methanol and some reactions of free radicals. For example, the emission of CN radicals in

CH_3OH/Ar plasma is from the reaction of hydrocarbon radicals with N_2 molecules from ambient air. The CH band may come from the methanol dissociation. Furthermore, the CN emission band and C_2 Swan band, especially C_2 Swan band, may indicate the carbon deposition in the plasma discharge. Besides, there is almost no evidence of atomic oxygen lines (777.3 nm and 844.6 nm) in Fig. 4(a) which would come from the dissociation of oxygen molecule and OH radical self-recombination, which may demonstrate that the contribution of water molecule dissociated by O(1D) (reaction 3) to the OH radical production in a plasma jet is negligibly small.

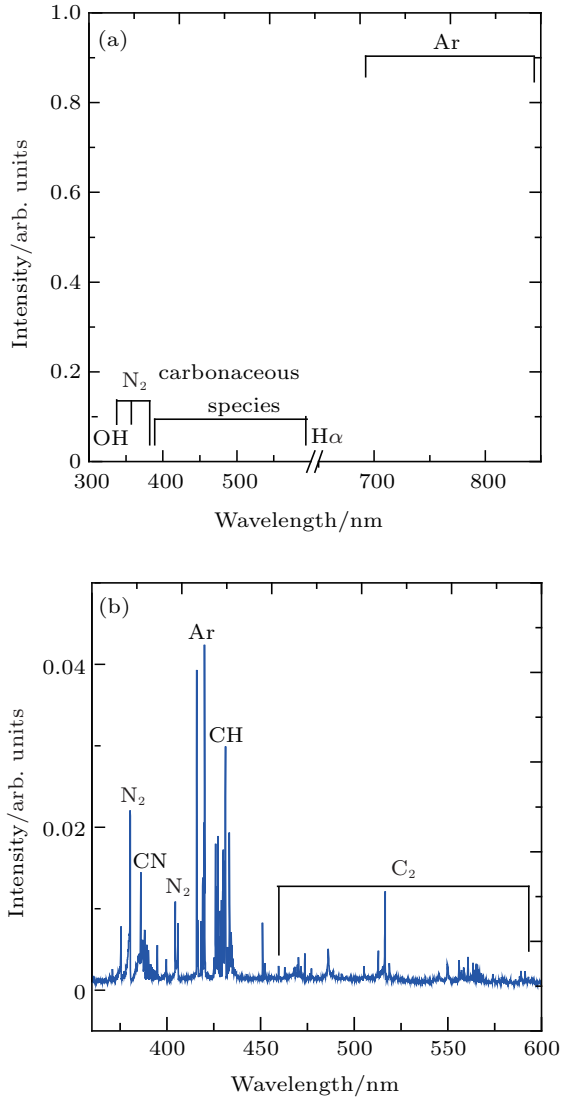


Fig. 4. (color online) Optical emission spectra in ranges of (a) 300 nm–850 nm and (b) 325 nm–600 nm of the CH_3OH–Ar plasma jet with CH_3OH/Ar ratio of 0.1%.

3.2. Variations of OH density

An improved OH radical decay model is proposed to obtain the absolute density of OH radicals in APPJ,[14–16] in which both main OH loss mechanisms produced by chemical reaction and the effect of gas flow are considered. More detailed descriptions of this OH decay model can be found in our previous reports. However, in our work, the reaction-rate data for the OH loss reactions in CH_3OH/Ar plasma are unclear in the literature. For instance, the R14 reaction in Table 1 is considered as an important OH loss reaction pathway.[20,21] In order to avoid this problem, the possible loss mechanisms of OH are considered in pure argon. We compare the experimental OH LIF signal data at a series of delay times after the falling edge of the voltage pulse and the simulated OH decay curve. By this way, the absolute OH density in pure argon can be obtained when a best fit between the two profiles is reached. Then, the absolute OH density in the CH_3OH/Ar plasma jet can be deduced due to the fact that the integrated OH LIF intensities at different CH_3OH/Ar volume ratios are proportional to the absolute OH densities. In order to better control the OH density in the CH_3OH/Ar plasma jet, the variations of OH density with operating parameters, including applied voltage, pulse frequency, and pulsewidth, are simultaneously studied in the following.

Figure 5 shows the absolute OH density as a function of applied voltage. As can be seen, the OH density for the case of applied voltage of 4.0 kV is about 7.8×10^{12} cm^{-3}. As the applied voltage is increased to 9.0 kV, the OH density increases to more than 3.7×10^{13} cm^{-3}. Besides, the OH density increases linearly with the applied voltage ranging from 4.0 kV to 9.0 kV. One can infer that the power absorbed by plasma may also increase with applied voltage in this range. Thus, the discharge parameters, such as electron temperature, electron density, and gas temperature, also increase linearly with applied voltage, thus causing the linear increase in OH density. OH radicals produced in the previous discharge pulse can accumulate, resulting in a strong pulse dependence of OH density. Therefore, we plot the absolute OH density versus pulse frequency in Fig. 6. As can be seen, as the pulse frequency increases from 0.5 kHz to 9 kHz, the OH density increases from 8.3×10^{12} cm^{-3} to 3.6×10^{13} cm^{-3}. It is worth noting that the OH density increases but not linearly with pulse frequency, which is ascribed to the decay of OH radicals from previous multiple voltage pulses.[15] Finally, the influence of pulsewidth on OH density is also presented in Fig. 7. It clearly shows that the absolute OH density is not sensitive to the variation of pulsewidth. As the pulsewidth is increased from 0.5 μs to 80 μs, OH density is found to be in a range of 3.2×10^{13} cm^{-3}–3.4×10^{13} cm^{-3}. According to our previous experimental results, the OH radicals in pulsed-dc plasma jet are mainly produced in the pulse rising and falling edges of applied voltage.[16] In the case of the maximum pulse width of 80 μs in our work, this short time has no obvious effect on the decay of OH radicals. Therefore, there is no significant difference of OH density on pulse width.

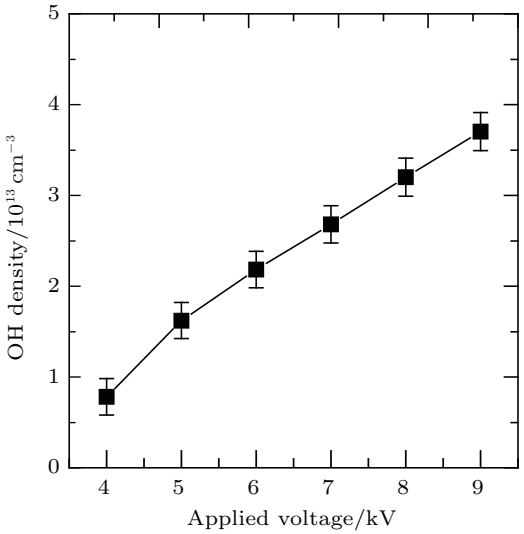


Fig. 5. Variation of absolute OH density with applied voltage magnitude.

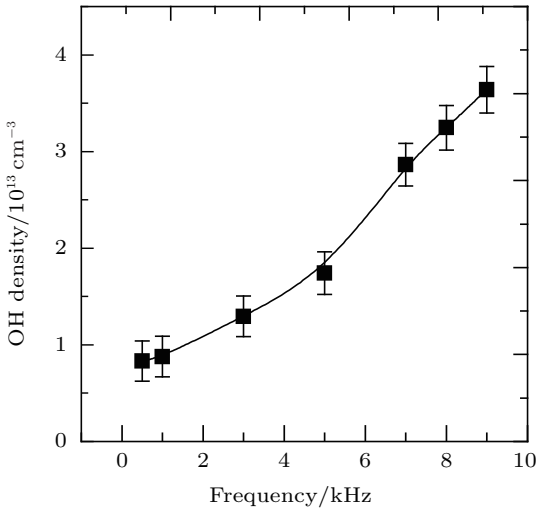


Fig. 6. Variation of absolute OH density with pulse frequency.

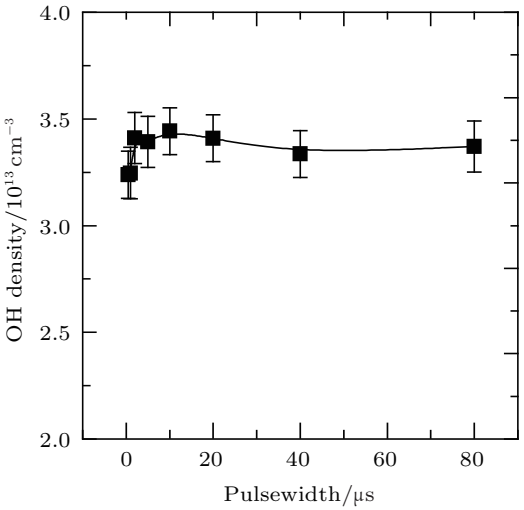


Fig. 7. Variation of absolute OH density with pulse width.

4. Conclusions

In this work, we present LIF and OES measurements of an atmospheric-pressure CH_3OH/Ar plasma jet. It is shown that OH LIF emission is relatively uniform in the needle-to-ring discharge gap. However, OH LIF signals show the ring-shaped distribution in the afterglow of plasma jet. Besides, the OH LIF emission intensity inside the nozzle is stronger than that in the afterglow of plasma jet. Distinct types of space-resolved behaviors of OH LIF emission may be attributed to the different production mechanisms of OH radicals. In detail, OH radicals in the far afterglow of a plasma jet are mainly produced from the reactions of water dissociation with metastables (Ar^m and N_2^m). However, OH radicals in the needle-to-ring discharge gap are mostly generated from methanol vapor and water molecules dissociations. Three characteristic carbonaceous species, CN, CH, and C_2 are detected in the CH_3OH/Ar plasma by OES. Furthermore, the OH density increases linearly with applied voltage but nonlinearly with frequency. Pulse width has no significant influence on OH density.

References

[1] Xiong Z, Zhao S, Mao X, Lu X, He G, Yang G, Chen M, Ishaq M and Ostrikov K 2014 *Stem Cell Res.* **12** 387

[2] Fridman G, Friedman G, Gutsol A, Shekhter A, Vasilets V and Fridman A 2008 *Plasma Processes Polym.* **5** 503

[3] Iza F, Kim G, Lee S, Lee J, Walsh J, Zhang Y and Kong M 2008 *Plasma Processes Polym.* **5** 322

[4] Yang D Z, Li J, Wang W C, Wang S, Jiang P C, Zhang S, Qing X Y and Chen G L 2014 *Plasma Processes Polym.* **11** 842

[5] Duarte S, Kuo S P, Murata R M, Chen C Y, Saxena D, Huang K J and Popovic S 2011 *Phys. Plasmas* **18** 073503

[6] Xiong Q, Lu X P, Ostrikov K, Xian Y, Zou C, Xiong Z and Pan Y 2010 *Phys. Plasmas* **17** 043506

[7] Zhang J, Yuan Q C, Zhang J L, Li T and Guo H C 2013 *Chem. Commun.* **49** 10106

[8] Bruggeman P, Cunge G and Sadeghi N 2012 *Plasma Sources Sci. Technol.* **21** 035019

[9] Verreycken T, Mensink R, van der Horst R, Sadeghi N and Bruggeman P 2013 *Plasma Sources Sci. Technol.* **22** 055014

[10] Ono R and Oda T 2003 *J. Appl. Phys.* **93** 5876

[11] Ono R and Oda T 2008 *J. Phys. D: Appl. Phys.* **41** 035204

[12] Li L, Nikiforov A, Xiong Q, Britun N, Snyders R, Lu X and Leys C 2013 *Phys. Plasmas* **20** 093502

[13] Qian M Y, Yang C Y, Wang Z D, Chen X C, Liu S Q and Wang D Z 2016 *Chin. Phys. B* **25** 015202

[14] Liu X Y Pei X K, Ostrikov K, Lu X P and Liu D W 2014 *Phys. Plasmas* **21** 093513

[15] Pei X K, Wu S Q, Xian Y, Lu X P and Pan Y 2014 *IEEE Trans. Plasma Sci.* **42** 1206

[16] Pei X, Lu Y, Wu S, Xiong Q and Lu X 2013 *Plasma Sources Sci. Technol.* **22** 025023

[17] Yonemori S and Ono R 2014 *J. Phys. D: Appl. Phys.* **47** 125401

[18] Liu D X, Bruggeman P, Iza F, Rong M Z and Kong M G 2010 *Plasma Sources Sci. Technol.* **19** 025018

[19] Han Y, Wang J G, Cheng D G and Liu C J 2006 *Ind. Eng. Chem. Res.* **45** 3460

[20] Hiroki A, Pimblott S M and Laverne J A 2002 *J. Phys. Chem. A* **106** 9352

[21] Yan Z C, Chen L and Wang H L 2007 *Acta Phys.-Chim. Sin.* **23** 835 (in Chinese)

[22] Chang A H H and Lin S H 2002 *Chem. Phys. Lett.* **363** 175